Article

Near- and Mid-Infrared Graphene-Based Photonic Architectures for Ultrafast and Low-Power Electro-Optical Switching and Ultra-High Resolution Imaging

Vincenzo Caligiuri,* Alessandro Pianelli, Mario Miscuglio, Aniket Patra, Nicolò Maccaferri, Roberto Caputo,* and Antonio De Luca*

Cite This: https://dx.doi.org/10.1021/acsanm.0c02690

Read Online

ACCESS | Metrics & More | Article Recommendations | Supporting Information

ABSTRACT: Confining near-infrared (NIR) and mid-infrared (MIR) radiation (1−10 μm) at the nanoscale is one of the main challenges in photonics. Thanks to the transparency of silicon in the NIR-MIR range, optoelectronic systems like electro-optical modulators have been broadly designed in this range. However, the trade-off between energy-per-bit consumption and speed still constitutes a significant bottleneck, preventing such a technology to express its full potentialities. Moreover, the harmless nature of NIR radiation makes it ideal for bio-photonic applications. In this work, we theoretically showcase a new kind of electro-optical modulators in the NIR-MIR range that optimize the trade-off between power consumption, switching speed, and light confinement, leveraging on the interplay between graphene and metamaterials. We investigate several configurations among which the one consisting in a SiO$_2$/graphene hyperbolic metamaterial (HMM) outstands. The peculiar multilayered configuration of the HMM allowed one also to minimize the equivalent electrical capacitance to achieve attoJoule electro/optical modulation at about 500 MHz switching speed. This system manifests the so-called dielectric singularity, in correspondence to which an HMM lens with resolving power of λ/1660 has been designed, allowing to resolve 3 nm-wide objects placed at an interdistance of 3 nm and to overcome the diffraction limit by 3 orders of magnitude. The imaging possibilities opened by such technologies are evident especially in bio-photonic applications, where the investigation of biological entities with tailored/broadband-wavelength radiation and nanometer precision is necessary. Moreover, the modulation performances demonstrated by the graphene-based HMM configure it as a promise for ultrafast and low-power opto-electronics applications.

KEYWORDS: graphene, HMM, hyperbolic metamaterials, metal/insulator architectures, light confinement, ultrafast, all-optical switching
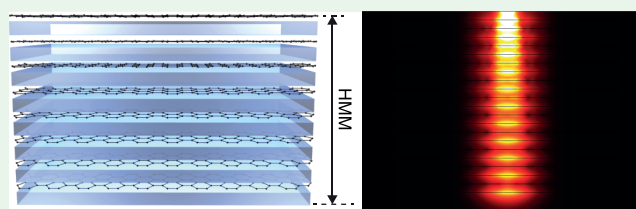
INTRODUCTION

Near- and mid-infrared radiation (1−10 μm) is often selected as the ideal framework for the design of optoelectronics systems. This is mainly due to the transparency of silicon in this spectral range.[1−3] Silicon represents, indeed, often the material of choice in optoelectronics due to its low cost and availability and since its use allows one to fabricate devices via the broadly used CMOS process. Silicon-based high-speed photonic devices in the NIR-MIR band have, therefore, spread in the technology scenario, and among them, electro-optical modulators play a very important role.[4] The NIR-MIR spectral region is also very important in optical telecommunications[5] and for bio-photonics applications. It is indeed well known that radiation with wavelength longer than 900 nm can efficiently penetrate biological tissues as blood and skin.[6,7] Techniques like Fourier transform infrared spectroscopy (FTIR) or Raman scattering involving radiation in the MIR range are also very common in biology since many bio-fingerprints like molecular vibrations lie in this spectral region.[8−11] Particularly interesting is the so-called "second near-infrared (NIR-II) window"

between 1000 and 1700 nm, which is often the investigation band of choice for biological applications, due to the absence of autofluorescence phenomena.[12,13] Thanks to the significant steps forward made in the fabrication of biocompatible fluorophores emitting in the NIR-II region, techniques like "in vivo NIR fluorescence imaging" are emerging.[14−16] Imaging techniques that leverage on nonlinear effects, like two-photon spectroscopy, are also widely used, but they necessitate expensive and/or toxic highly nonlinear materials as labels.[17−19] The core of all these techniques is, however, a classical optical apparatus, usually a confocal microscope, whose resolution is diffraction-limited. The maximum resolution achievable by confocal microscopy is in the order
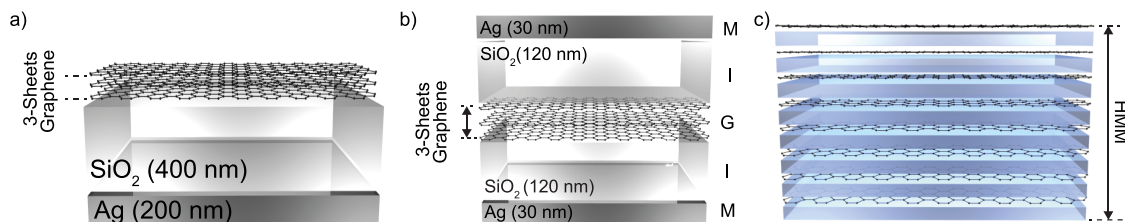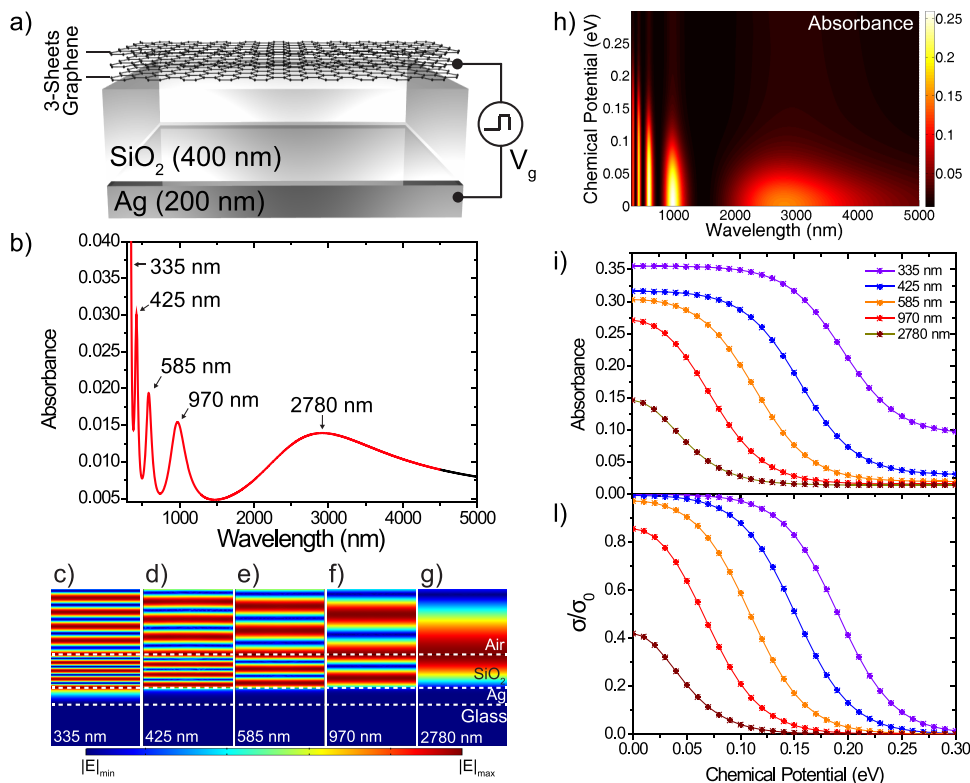
Figure 1. Sketch of (a) the insulator/metal (IM) SiO$_2$/Ag bilayer with the three-sheet graphene switching layer placed on the top, (b) the MIGIM structure with graphene embedded in the middle, and (c) the graphene/SiO$_2$ HMM.

Figure 2. (a) Sketch of the graphene/insulator/metal (GIM) architecture made of a three-sheet graphene layer and 400 nm SiO$_2$ and 200 nm Ag layers. (b) Modes sustained by the pristine Ag/SiO$_2$ IM structure. (c–g) Modulus (|E|) of the electric field for all the modes calculated *via* COMSOL simulations. (h) Map showing the switching of the modes of the GIM structure while increasing the applied chemical potential. (i) Absorbance value at the resonances of the GIM structure showing a logistic switch-off trend, driven by (l) the modulation of the real part of the normalized conductivity of the graphene layer induced by changing its chemical potential.

of 0.61 λn/NA, being NA the numerical aperture of the objective and n the refractive index of the medium between the lens and the specimen.[3] To give an example at a wavelength that will be of interest in this paper, if a confocal investigation is carried out at 4985 nm with a high-quality immersion objective with NA = 1.4 and n (immersion oil) = 1.5, the maximum resolution achievable is of about 3.25 μm (λ/1.53). In this paper, we show how to design architectures capable to increase such a value by at least 3 orders of magnitude by leveraging on the interplay between graphene and metamaterial optical response/conductivity. The use of graphene in combination with plasmonic structures has, indeed, already demonstrated its potentialities in several frameworks, and[20−23] as an additional advantage, the presence of graphene endows the proposed structures with broadband electric tunability so that their optical response can be switched at will by changing the chemical potential of the graphene layers. In particular, we investigate graphene-based optical resonators whose structural complexity is gradually improved from a single graphene/

insulator/metal (GIM) unit cell (Figure 1a), passing by a metal/insulator/graphene/insulator/metal (MIGIM) resonator (Figure 1b), toward a complete graphene-based hyperbolic metamaterial (HMM, Figure 1c). Each one of the proposed structures is thought to optimize a particular parameter in the trade-off between light confinement, switching speed, and energy/bit consumption, and therefore, several variants of these configurations are analyzed in the paper.

The most promising configuration investigated in the paper is the graphene/SiO$_2$ hyperbolic metamaterial (HMM) sketched in Figure 1c, designed to support a tunable dielectric singularity where the so-called canalization regime can be easily achieved.[24] In this configuration, the HMM shows outstanding performances as a plasmonic near-field lens with a resolution of about λ/1660, which allows the investigation of nanometric elements (∼3 nm) positioned at nanometric distances (∼3 nm) with MIR radiation (4985 nm). Moreover, we found that the peculiar multilayered architecture together with the narrow-band nature of the dielectric singularity

constitutes the perfect combination for achieving attoJoule modulation with a switching speed of around 500 MHz.

RESULTS AND DISCUSSION

Switching of Pseudo-Cavity and Plasmonic Modes in Graphene/Insulator/Metal (GIM) Structures. The first system considered in our analysis is based on a simple insulator/metal (IM) SiO_2/Ag bilayer. Depending on the thickness of the dielectric layer, such a system sustains modes of different nature. A detailed analysis of the modal dispersion of the IM structure as a function of the thickness of both the metal and the dielectric layers is provided in Section S-2 of the Supporting Information. In particular, it is found that, for SiO_2 layers thicker than 50 nm, the modal dispersion of the IM structure is linear, similar to a classic Fabry−Pérot resonator. A noticeable difference explained in Section S-2 of the Supporting Information between the IM structure and a classic Fabry−Pérot is that, in the IM structure, modes can be excited every time the phase difference between an impinging wave and a second wave that accumulated a complete cavity roundtrip phase shift is an integer multiple m of π. In the case in which m is odd, destructive interference occurs and the modes are sustained via a frustrated total internal reflection regime, while when m is even, the condition for a classic Fabry−Pérot mode is fulfilled. We can conveniently refer to these modes, excited for a SiO_2 thickness larger than 50 nm, as pseudo-cavity modes. If the thickness of the SiO_2 layer is smaller than 50 nm, the pseudo-cavity mode relation is no more satisfied, and the modes are sustained by the excitation of surface plasmons. The simple IM structure can be made active by depositing on top of it a three-sheet graphene layer, as illustrated in Figure 2a. In particular, Ag is 200 nm-thick while the thickness of the SiO_2 layer is 400 nm so that the modes excited in the pristine IM bilayer, calculated via the scattering matrix method (SMM) (Figure 2b), are pseudo-cavity modes. Five modes are present at 335, 425, 585, 970, and 2780 nm. To rule out any plasmonic contribution, we calculated the modulus of the electric field ($|E| = \sqrt{E_x^2 + E_y^2}$) via full-wave finite element method-based simulations (COMSOL Multiphysics), finding that these modes hold the features of those confined in classic metal/insulator/metal (MIM) cavities,[25,26] with the exception that, due to the missing top metal, a substantial portion of the electric field of the mode lies at the air/dielectric interface. For example, a closer inspection to Figure 2g reveals that the fundamental mode ($m = 1$) at 2780 nm reaches the maximum at the boundary between the SiO_2/air interface and decays in air. This feature is present in all the modes (Figure 2c−g). Placing a three-sheet graphene layer on top of the pristine IM bilayer does not produce any spectral modification of the modes. However, despite its negligible thickness, the effect of the three-sheet graphene layer on the absorbance value at each mode is significant. Indeed, while changing the chemical potential of the top graphene layer via electrical doping, the absorbance of all the modes undergoes a significant reduction, as shown in the map of Figure 2h. Noticeably, the switching trend of the absorbance of the modes as a function of the chemical potential applied to the graphene layer follows a logistic slope (Figure 2i) that is the same as that of the conductivity of graphene at their wavelengths (Figure 2l).

Optimization of the Switching Performances of Graphene/ Insulator/Metal (GIM) Structures. The simple

GIM configuration offers a very advantageous trade-off between design complexity, light confinement, and switching performances. Moreover, it constitutes the fundamental building block toward the more sophisticated configurations that will be shown after so that a deep understanding of this simple element as an electro/optical modulator is insightful. Regarding the electrostatics, the performances of an electro/optical modulator are usually expressed in terms of (i) switching frequency, (ii) back-gate voltage, and (iii) energy/bit consumption. The switching frequency is the cutoff frequency of the RC circuit associated with the electrical gating configuration of the device that can be expressed as in eq 1:

$$f_{-3dB} = \frac{1}{2\pi RC} \tag{1}$$

being R the discharging resistance whose main contribution is given by the ohmic nature of the contacts. In this work, R is always taken to be equal to 1 kΩ. Such a value is plausible considering the contact resistance and the deposition over SiO_2, and it allows one to account a good approximation for the series resistances associated with each equivalent RC circuit. C is the equivalent capacitance related to the particular configuration of the electro/optical modulator. Throughout the paper, the electrical configuration always resembles that of one or a series of flat parallel-plate capacitors. Therefore, for the single capacitor, $C = \varepsilon_0 \varepsilon_r \frac{S}{d}$, being ε_0 the vacuum dielectric permittivity expressed in Section S-1 of the Supporting Information and ε_r the relative dielectric permittivity of SiO_2 that, in the gigahertz range (modulation frequency range), can be taken to be equal to 4. S is the surface of the capacitor that can be considered equal to 10^{-10} m^2 (a square of 10 μm × 10 μm), and d is the separation distance either between the graphene layer and the bottom Ag layer or two facing graphene layers. Replacing the relation of the capacitance in eq 1, we obtain:

$$f_{-3dB} = \frac{d}{2\pi R \varepsilon_0 \varepsilon_r S} \tag{2}$$

A quick inspection of eq 2 brings to the conclusion that the route to maximize the switching speed of a parallel-plate capacitor electro/optical modulator passes by (i) reducing the series resistance R, (ii) reducing the relative dielectric permittivity of the oxide, (iii) reducing the surface S, and (iv) increasing the thickness d of the capacitor. However, a stringent trade-off appears when considering the back-gate voltage to apply to reach the electrical doping of graphene suitable to induce the desired chemical potential. The back-gate voltage can be expressed as follows:[27−30]

$$V_g = \frac{d \cdot e}{\pi \varepsilon_0 \varepsilon_r} \left(\frac{\mu_c}{\hbar \cdot \nu_f} \right)^2 \tag{3}$$

where e is the electron charge, $\hbar$ is the reduced Planck constant, and ν_f is the Fermi velocity. Equation 3 shows that the route to maximize the switching frequency is also a path for very high back-gate voltages. Indeed, eq 3 hides a capacity per unity surface since $\frac{d}{\varepsilon_0 \varepsilon_r} = \left(\frac{C}{S} \right)^{-1}$. In light of this, the trade-off between switching speed and back-gate voltage is clear, minimizing the capacity results detrimental for both the switching speed and the back-gate voltage. In the end, the
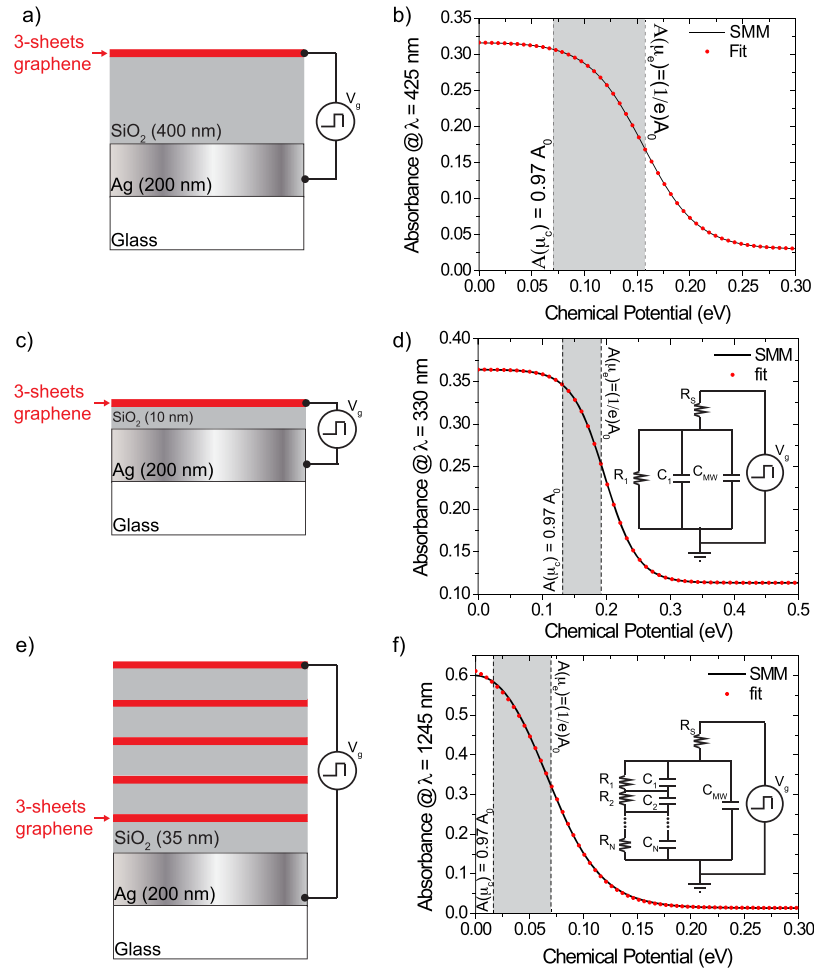
Figure 3. (a) Sketch and electrical gating scheme of the graphene/insulator/metal (GIM) architecture made of a three-sheet graphene layer, 400 nm SiO$_2$ layer, and a 200 nm Ag back reflector. (b) Calculated switching of the absorbance mode at 425 nm (solid black curve) together with the fitting curve (red dots). (c) Sketch and electrical gating scheme of the graphene/insulator/metal (GIM) architecture made of a three-sheet graphene layer, 10 nm SiO$_2$ layer, and a 200 nm Ag back reflector. (d) Calculated switching of the absorbance mode at 330 nm (solid black curve) together with the fitting curve (red dots). In the inset, the equivalent circuit referred to (a) and (c). (e) Sketch and electrical gating scheme of the graphene/insulator/metal (GIM) multilayered architecture made of five bilayers of three-sheet graphene and 35 nm SiO$_2$ and a 200 nm Ag back reflector. (f) Calculated switching of the absorbance mode at 1245 nm (solid black curve) together with the fitting curve (red dots).

energy accumulated in one charge cycle can be calculated as follows:

$$E_g = \frac{1}{4}CV_g^2 \tag{4}$$

Switching from one chemical potential to another requires switching between two values V_{g-on} and V_{g-off} of back-gate voltage, with a consequent energy consumption per bit ΔE_g equal to:

$$\Delta E_g = \frac{1}{4}C(V_{g-on} - V_{g-off})^2 \tag{5}$$

From eq 5, it turns out that, to minimize the switching energy, a low value of $\Delta = (V_{g-on} - V_{g-off})$ is crucial. On an optical point of view, the three main figures of merit (FOM) are (i) the insertion loss (IL), intended as losses in dB associated to the off state of the modulator; (ii) the extinction ratio (ER) that represents the difference in dB between losses in the on and off states of the modulator; and (iii) the ratio ER/IL. However, in our case, the thick bottom metal does not allow one to work in transmission and the IL has to be

replaced with its reflection counterpart usually called return loss (RL):

$$RL = -20 \cdot Log(S_{22}) \tag{6}$$

where S_{22} is the scattering parameter associated with the reflectivity of the structure when the modulator is in the off state. Since, in the structures considered in this section, the transmission can always be assumed to be close to zero, the reflectance is equal to 1-absorbance and eq 6 can be conveniently expressed in terms of the absorbance:

$$RL = 20 \cdot Log(1 - A_{off}) \tag{7}$$

being A_{off} the absorbance of the modulator in the off state. The ER can be calculated as follows:

$$ER = 20 \cdot Log\left(\frac{1 - A_{on}}{1 - A_{off}}\right) \tag{8}$$

Let us begin with the simple case of the switching of the pseudo-cavity modes illustrated in Figure 2i,l. The gating configuration for this particular case is the one shown in Figure

Table 1. Electrical and Optical Performances of the Systems Described in Figure 3a,c,e

	switching frequency	λ (nm)	V_{g-on} (V)	V_{g-off} (V)	energy/bit	capacitance (fF)	RL (dB)	ER/RL
GIM (Figure 3a)	~15 GHz	425	6.5	32	2 pJ/Bit	~9	1.77	0.8
GIM (Figure 3c)	~450 MHz	330	0.56	1.2	36 fJ/Bit	355	2.54	0.46
multilayer GIM (Figure 3e)	~40 GHz	1245	0.13	2.85	40 fJ/Bit	20	3.35	1.27

3a, while the equivalent circuit is the one shown in the inset of Figure 3d. Here, the series resistance $R_s = 1$ kΩ and being the value of R_1 negligible with respect to R_s, its value has been embedded within it. The capacitance C_{MW} is the so-called Maxwell−Wagner capacitance that is negligible in the gigahertz range.[31] The thick oxide layer (400 nm) ensures a small capacity (~9 fF) to which a high switching speed of ~15−20 GHz is associated. It has been shown in Figure 2i that the switching of the modes follows a logistic curve tracing the footprint of the Fermi−Dirac distribution function. Therefore, the dependence of the absorbance on the chemical potential shows a typical logistic trend that allows us to fit the absorbance curves of Figure 2i with a classic logistic curve following the Boltzmann distribution:

$$A(\mu_c) = \frac{A_0 - A_{fin}}{1 + e^{(\mu_c - \mu_e)/t}} + A_{fin} \tag{9}$$

For the mode at 425 nm, A_0 and A_{fin} are the absorbance values at $\mu_c = 0$ eV and $\mu_c = 0.3$ eV, respectively, μ_c is the varying chemical potential, t is the decay constant that can be conveniently measured in eV per absorbance unit since it determines the slope of the absorbance variation while increasing the chemical potential, and, most importantly, μ_e is the chemical potential at the center of the logistic curve. In this case, μ_e is also the value at which the absorbance value is decreased by a $1/e$ factor with respect to its starting value. The results of the fit are compared with the original curve in Figure 3b. The fitting parameters for the absorbance curve at 425 nm of Figure 3b are as follows: $A_0 = 0.317$, $A_{fin} = 0.03$, $t[\text{eV/abs} - \text{unit}] = 0.026$, and $\mu_e[\text{eV}] = 0.156$.

The modulation can, therefore, be carried out by switching the system of Figure 3a between $\mu_{c-off} = 0.07$ eV ($A_0 \cdot 0.97$, off state) and $\mu_e = 0.156$ eV (A_0/e, on state), with $\Delta\mu = 0.086$ eV. We obtain $\Delta E_g \approx 2$ pJ/bit and $V_{g-on} = V_g(\mu_e) = 32$ V and $V_{g-off} = V_g(\mu_c = 0.07$ eV$) = 6.5$ V. From the optical point of view, this modulator shows a noticeable ER/IL ratio of ~0.8, together with a very low RL = 1.77 dB. One way to reduce the back-gate voltage is to reduce the thickness of the oxide. To this aim, the plasmonic modes sustained by the IM bilayer are ideal since they are confined in a very thin dielectric layer. It should be said here that working with nanometrically thin oxide layers introduces gate leakage currents whose effect can be mitigated if a so-called high-k dielectric is used. In our analysis, however, we can neglect this effect since the driving voltages are sufficiently low to ensure the validity of the calculations. From the analysis carried out in Section S-2 of the Supporting Information, it turns out that the IM structure sustains modes at ~330 nm confined at the interface between Ag and the 10 nm-thick SiO$_2$ dielectric layer. The gating configuration is the one shown in Figure 3c, while in Figure 3d, the switching trend of the 330 nm mode is reported. Once more, the mode switching follows a logistic trend that can be fitted through eq 9 with the following parameters (absorbance curve at 330 nm of Figure 3d): $A_0 = 0.36$, $A_{fin} = 0.11$, $t[\text{eV/abs} - \text{unit}] = 0.026$, and $\mu_e[\text{eV}] = 0.198$.

The electrical and optical figures of merit can be calculated by following the same procedure as before. The switching speed is ~450 MHz. This value is lower than that of the previous configuration due to the increased capacity of ~355 fF resulting from the thin oxide. On the other hand, as expected, the back-gate voltages are significantly lowered between 0.56 V (off state) and 1.2 V (on state). Moreover, the switching energy results in more than 1 order of magnitude lowered ($\Delta E_g \approx 36$ fJ/bit). The RL value for this structure is ~2.54 dB with an ER/RL ratio equal to 0.46. If, on one hand, the previous configuration solves the problem of the back-gate voltage and switching energy, it has the main drawback of operating in the UV range. A wise way to move the operative wavelengths toward the infrared while keeping a sufficiently high switching speed and low energy consumption is to stack multiple graphene/SiO$_2$ bilayers on top of Ag, as shown in Figure 3e. From the optical point of view, this is equal to consider an effective dielectric with increased thickness with the benefit of moving the resonance toward the red spectral range to access the optical telecommunication band (O-band). From the electrical point of view, the equivalent capacitance seen between the two electrodes is the series of as many capacitances as the number N of graphene/SiO$_2$ bilayers. Since all the capacitances are equal to each other, the equivalent capacitance results equal to C/N, being C the capacitance of the single graphene/SiO$_2$/graphene cell. To this aim, we consider a stack of $N = 5$ graphene/SiO$_2$ bilayers on top of Ag. Here, SiO$_2$ is 35 nm-thick. The resulting multilayer shows a mode at 1245 nm at the high-energy edge of the O-band of the optical telecommunication range. This mode can be switched on and off as well while increasing the voltage between the two electrodes, showing the typical logistic slope that can be fitted via eq 9, as shown in Figure 3f. For this particular mode (at 1245 nm of Figure 3f), the fitting parameters are as follows: $A_0 = 0.64$, $A_{fin} = 0.01$, $t[\text{eV/abs} - \text{unit}] = 0.025$, and $\mu_e[\text{eV}] = 0.07$.

The equivalent circuit associated with this configuration is sketched in the inset of Figure 3f. It is important to point out here that the equivalent circuit proposed in the following description is used to characterize only the electrostatic behavior and in no way is related to the optical properties of the structure. The equivalent capacitance seen between the electrodes is equal to 20 fF, the lowest among the analyzed graphene/IM configurations. Such a low capacitance allows us to reach a remarkable switching speed of ~40 GHz. The switching range can be readily obtained from the fit, lying between 0.13 V (off state) and 2.85 V (on state) associated with a switching energy consumption of ~40 fJ/bit. From an optical point of view, this configuration shows a remarkable ER/RL ratio of 1.27, mainly due to the high ER associated with the curve of Figure 3f. The performances of the structures illustrated in Figure 3a,c,e are summarized in Table 1.

Metal/Insulator/Graphene/Insulator/Metal Structures. A more efficient way to confine light is provided by metal/insulator/metal (MIM) cavities. The system we consider in this section is made of a Ag/SiO$_2$/Ag MIM in
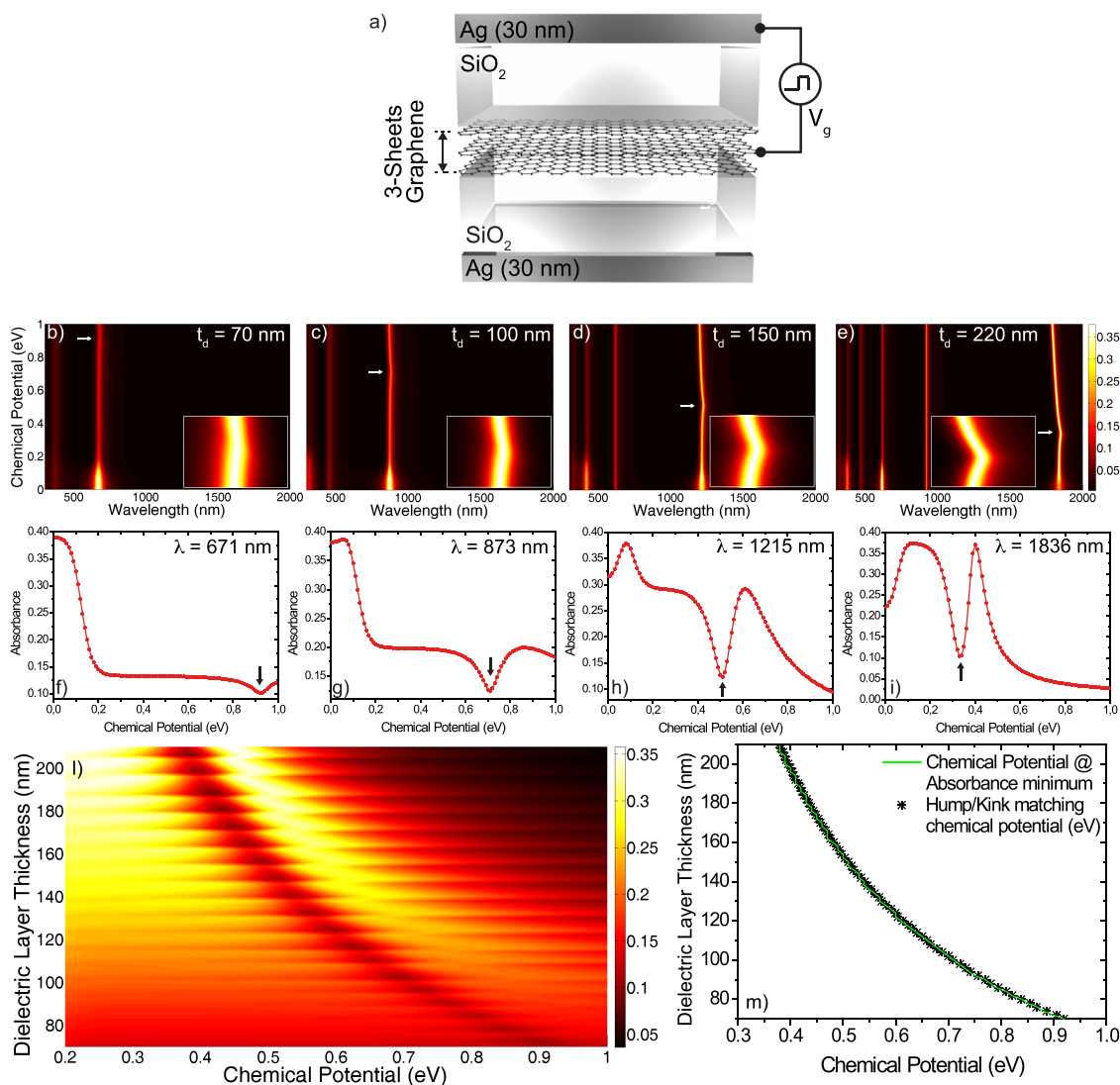
Figure 4. (a) Sketch of the MIGIM system highlighting the gating configuration. Absorbance map as a function of the chemical potential for graphene-embedded MIM cavities in which the thickness of the SiO$_2$ layers is equal to (b) 70 nm, (c) 100 nm, (d) 150 nm, and (e) 220 nm. The white arrows highlight the position of the absorbance kink, while the associated insets show a zoom around the kink. (f−i) Absorbance plots at the resonances associated with each SiO$_2$ thicknesses shown in (b)−(e). In (f)−(i), the local absorbance minimum associated with the presence of the kink is well distinguishable for a particular chemical potential, highlighted with a black arrow. (l) Map showing the chemical potential at which the kink manifests as a minimum in absorbance for a particular cavity mode (i.e., the thickness of SiO$_2$ layer). (m) Comparison between the chemical potential at which the kink occurs for a specific cavity mode (i.e., the thickness of SiO$_2$ layer; green curve) and the chemical potential that produces a local maximum in the real permittivity of the bare graphene at the same wavelength of the cavity mode (i.e., the thickness of SiO$_2$ layer; black stars). The perfect matching confirms that the local maximum in the real dielectric permittivity of graphene is responsible for the kink in absorbance.

which the three-sheet graphene layer is embedded in the middle of the dielectric layer to obtain a metal/insulator/graphene/insulator/metal (MIGIM) stack, as sketched in Figure 4a.

Here, Ag is 30 nm. The optical response of the MIGIM is very similar to that of a MIM, but despite the exiguous thickness of the graphene layer, its influence in the dispersion of the cavity mode is significant. In the map of Figure 4b−e, it is shown the modification of the absorbance of the MIGIM structure while increasing the thickness of each of the two SiO$_2$ layers between 70 nm (Figure 4b), 100 nm (Figure 4c), 150 nm (Figure 4d), and 220 nm (Figure 4e). Each panel reports the associated dependence of the absorbance on the chemical potential of the graphene layer. As in the case of common MIM cavities, the peak in absorbance corresponds to a

resonance, red-shifts while increasing the thickness of the cavity.[25,32−34] As shown in Figure 4b−e, by increasing the chemical potential, the absorbance value at the resonant wavelength can be strongly attenuated, allowing to turn the modes on and off within the first 0.2 eV. Moreover, a closer inspection of Figure 4b−e reveals a kink in the absorbance peak, highlighted with a white arrow, occurring at different chemical potentials for different SiO$_2$ thicknesses. In the inset of each panel, a zoom around the kink is reported. The spectral deviation of the resonance occurring at the kink results in an absorbance minimum at a specific chemical potential (high-lighted with a black arrow in Figure 4f−i). Therefore, the chemical potential at which the kink occurs for a specific resonant wavelength (i.e., dielectric layer thickness) can be identified as the local absorbance minimum in the map of
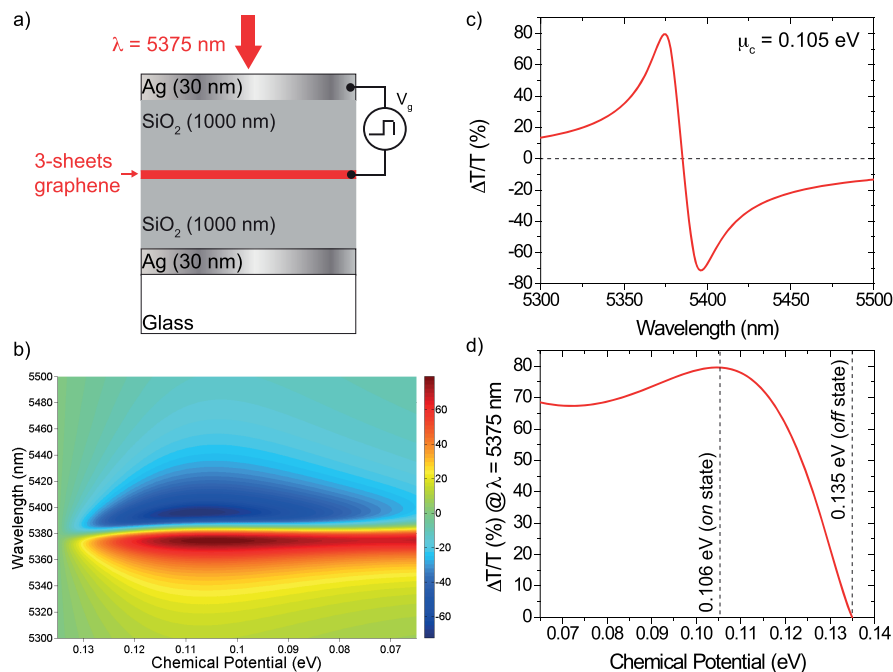
Figure 5. (a) Sketch of the Ag/SiO$_2$/graphene/SiO$_2$/Ag (30 nm/1000 nm/1 nm/1000 nm/30 nm) MIGIM modulator, together with the wiring scheme. (b) Differential transmissivity $\Delta T/T$ (%) map around the kink spectral range. (c) Differential transmissivity $\Delta T/T$ (%) at μ_c = 105 eV, in correspondence to the modulation maxima. (d) Modulation depth $\Delta T/T$ (%) as a function of the chemical potential calculated at lambda = 5375 nm (positive $\Delta T/T$ maximum), showing the effective operation range.

Figure 4l. This complete portrait of the kink/μ_c trend sheds light on the origin of this behavior. The kink stems from the particular shape of the real part of the dielectric permittivity of the bare graphene that manifests a local maximum in the proximity of the epsilon-near-zero (ENZ) point (see the Materials and Methods and Figure S1a in the Supporting Information). When the wavelength of the local maximum in the real part of the permittivity matches the resonance of the MIGIM system, the effective permittivity of the "IGI" core layer of the cavity increases, inducing a red-shift of the resonance. This occurs only at a specific chemical potential. To confirm this, in Figure 4m, we compare the chemical potential at which the kink-driven absorbance minimum occurs for a specific cavity mode (i.e., dielectric layer thickness; green curve) with the chemical potential that produces the local maximum in the real permittivity of graphene at the same wavelength of the cavity mode (stars). The perfect matching between these two quantities confirms the explanation given before. Thanks to the versatility of this configuration and to the straightforward capability to modify their resonant wavelength, cavity modes occurring in MIM resonators have been recently employed as ultrafast (sub-3 ps) optical modulators.[35] The absorbance switching properties shown in Figure 4b−i can be exploited for this purpose as well. As an additional advantage, MIM resonators can be easily engineered to work in the NIR-MIR range, being this the spectral region of interest of this paper. The spectral modulation performances of a device can be evaluated in terms of the differential transmissivity $\frac{\Delta T}{T} = -\text{Log}\left(\frac{T(t)}{T(t_0)}\right)$, where $T(t)$ is the transmittance at a time t after the application of the modulation stimulus that, in our case, is a variation of the chemical potential, and $T(t_0)$ is the reference transmissivity at the starting point.[2,36−38] It is worth noticing that analogous figures of merit can be considered, associated to the other scattering parameters (i.e., differential reflectivity and absorbance), but for our purposes, detecting transmissivity is very convenient since it allows one to minimize the insertion loss and maximize the extinction ratio. Therefore, by considering a time-dependent modulation of the applied chemical potential, we can redefine the differential transmissivity as a function of the chemical potential rather than time as $\frac{\Delta T}{T} = -\text{Log}\left(\frac{T(\mu_{ci})}{T(\mu_{c0})}\right)$, where μ_{c0} is the starting chemical potential and μ_{ci} is the chemical potential at the ith instant. From eq 5, it follows that, to minimize V_g, both the chemical potential and the thickness of the capacitor have to be small. However, from Figure 4l,m, it turns out that the MIGIM configuration forces a trade-off between these two quantities. Indeed, to make the kink occur at lower chemical potentials, the thickness of the dielectric layers has to be increased. Therefore, since the dependence on the chemical potential in eq 5 is quadratic while the dependence on the thickness is linear, it is convenient to minimize μ_c at the price of a high d. As an additional benefit, the resonance is moved toward the IR range.

To keep μ_c below 0.2 eV, we set the thickness of the SiO$_2$ layers equal to 1000 nm, as sketched in Figure 5a, where the gating configuration is shown as well. The value $\Delta T/T$ calculated within the entire modulation range between 5300 and 5500 nm is provided in Figure 5b, revealing a modulation depth of about ±80% in the on state (μ_{c-on} = 0.106 eV) with respect to the off state (μ_{c-off} = 0.135 eV) as shown in Figure 5c. The energy/bit consumption needed to switch between μ_{c-off} and μ_{c-on} is about 3.5 fF/bit. These values are in line with high-performance systems recently reported in the literature.[2,39−41] Since this configuration is used in transmittance, it is possible to properly calculate the insertion loss parameter, expressed as

$$\text{IL} = 20 \cdot \text{Log}(T_{off}) \tag{10}$$

Table 2. Electrical and Optical Performances of the System Shown in Figure 5a

	switching frequency (GHz)	λ (nm)	V_{g-on} (V)	V_{g-off} (V)	energy/bit (pJ/bit)	capacitance (fF)	IL	ER/IL	depth (%)
MIGIM	~45	5375	37	60	2	3.5	1.62	0.95	±80
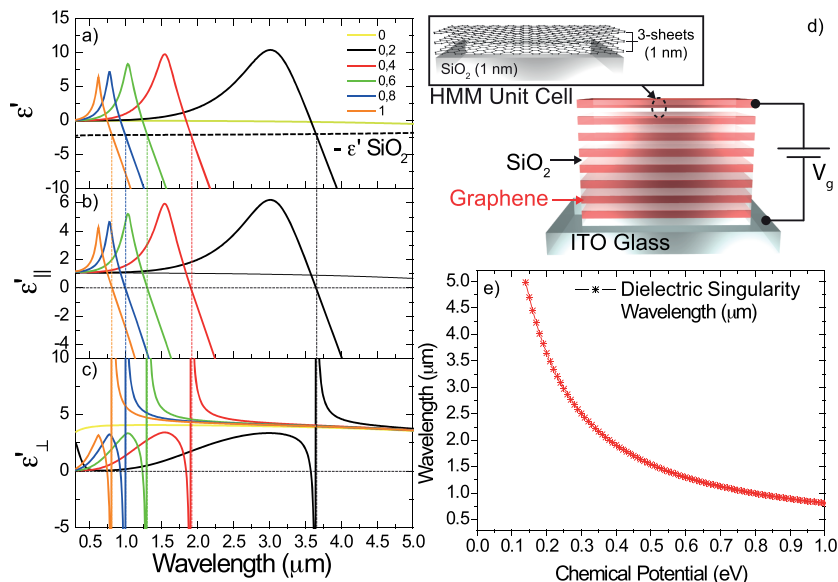
Figure 6. (a) Comparison between the real dielectric permittivity of graphene calculated at the chemical potentials indicated in the legend (in eV) and $-\varepsilon'_{SiO_2}$, highlighting the crossing wavelengths between them. Real (b) $\varepsilon_{\parallel}$ and (c) $\varepsilon_{\perp}$ of the graphene/SiO$_2$ 1/1 nm HMM. $\varepsilon_{\parallel}$ shows zeros where $\varepsilon_{\perp}$ manifests poles, confirming the occurrence of the dielectric singularity. (d) Sketch of the complete HMM (graphene corresponds to red layers while the white ones are SiO$_2$), together with a zoom within the unit cell made of a three-sheet (1 nm-thick) graphene layer on top of a 1 nm SiO$_2$ layer. (e) Dielectric singularity wavelengths as a function of the chemical potential.

which, in this case, is equal to 1.62 dB. The extinction ratio can be redefined as

$$\text{ER} = 20 \cdot \text{Log}\left(\frac{T_{on}}{T_{off}}\right) \tag{11}$$

and is equal to 1.54. The ER/IL ratio for this system is equal to 0.95. The performances of this architecture are resumed in Table 2.

Ultra-High-Resolution and Attojoule Modulation in Graphene/SiO$_2$ HMMs. If a suitable number of bilayers is provided, the graphene/SiO$_2$ multilayer forms a so-called hyperbolic metamaterial (HMM). HMMs are receiving always-growing attention in the frameworks of photonic and plasmonic technologies since their optical response can be easily engineered to sustain extreme propagation regimes and to enable unprecedented light confinement.[42−45] The most common HMM architecture consists of a metal/dielectric multilayer, whose local optical response can be described employing an effective uniaxial dielectric tensor. Its components are as follows:

$$\varepsilon_{\parallel} = \frac{t_d \varepsilon_d + t_m \varepsilon_m}{t_d + t_m} \tag{12}$$

$$\varepsilon_{\perp} = \frac{\varepsilon_d \varepsilon_m (t_d + t_m)}{t_m \varepsilon_d + t_d \varepsilon_m} \tag{13}$$

where t_d and t_m are the thickness of the dielectric and metallic layers, respectively, and ε_d and ε_m are their dielectric permittivities. If losses are negligible, when $t_d = t_m$ and $\varepsilon_m = -\varepsilon_d$, eq 12 manifests a zero while eq 13 a pole. Such a

condition is known as the canalization regime and the wavelength at which it occurs constitutes a so-called dielectric singularity representing the separation wavelength between two extremely anisotropic regimes called type I and type II.[24,46−48] In this regime, the HMM can be used as a near-field lens with a resolution far better than classic glass-based optics, limited mainly by the periodicity of the HMM.[24] The atomic thickness of graphene plays a crucial role in this view since it allows one to design HMMs with nanometric periodicity.[49] The particular HMM proposed hereafter consists of a stack of graphene, which plays the role of the metal, and SiO$_2$. Here, $t_d = t_m = t_{graphene} \approx 1$ nm, considering a three-sheet graphene layer. Figure 6a shows the real dielectric permittivity of graphene calculated at six different chemical potentials, compared with $-\varepsilon'_{SiO_2}$. The crossing points between $\varepsilon'_{graphene}(\mu_c)$ and $-\varepsilon'_{SiO_2}$ are those at which the condition $\varepsilon_m = -\varepsilon_d$ is fulfilled and correspond to the dielectric singularities occurring in the graphene/SiO$_2$ HMM at each chemical potential.

The real part of the effective parallel (eq 12) and perpendicular (eq 13) permittivities of the complete HMM made of 10 graphene/SiO$_2$ bilayers is shown in Figure 6b,c, respectively. In correspondence to the crossings points between $\varepsilon'_{graphene}(\mu_c)$ and $-\varepsilon'_{SiO_2}$ shown in Figure 6a, $\varepsilon_{\parallel}$ shows a zero while $\varepsilon_{\perp}$ a pole, confirming the occurrence of the canalization regime at those wavelengths. In Figure 6d, a sketch of the complete metamaterial is given, and in the inset, a zoom of the HMM unit cell, consisting in a three-sheet (1 nm-thick) graphene layer placed on top of a 1 nm SiO$_2$ layer, is depicted, showing also the electrical gating configuration. In this architecture, an ITO coated glass has to be used to ensure both transparency, essential for the lensing application, and
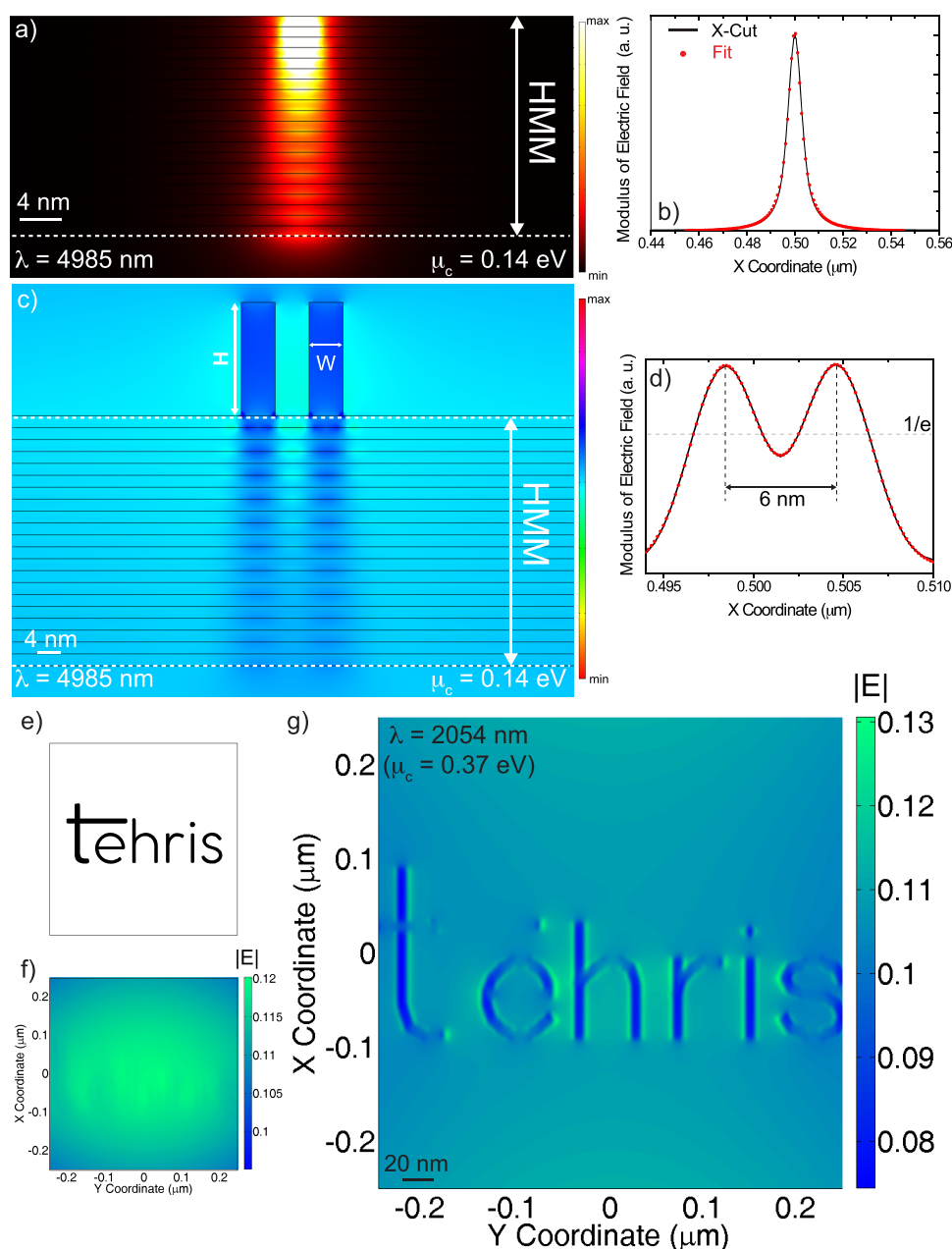
Figure 7. (a) Near-field modulus of the electric field (|*E*|) simulated by means of Lumerical Commercial software, obtained by exciting the graphene/SiO$_2$ HMM at the canalization wavelength of 4985 nm (0.14 eV). (b) |*E*| at the exit layer demonstrating a canalization factor of about λ/830. (c) |*E*| profile, showing the nanometric resolution of two SiO$_2$ rectangular objects placed on top of the HMM, separated by a 3 nm interdistance. (d) |*E*| at the exit layer demonstrating a resolving power of λ/1660 nm. (e) 3D logo "tehris" on top of the HMM to be resolved at the exit layer. (f) Imaging simulation conducted in the effective dielectric region (λ = 1000 nm) and (g) at the canalization wavelength λ = 2054 nm (0.37 eV), demonstrating a 3D resolution of more than λ/200.

conductivity for the electrical gating. Such a scenario is made possible by the recent advances in graphene deposition methods that allowed one to fabricate graphene-based conductive substrates using a variety of conductive layers.[50] The wavelengths at which the dielectric singularities occur are plotted in Figure 6e while varying the chemical potential, demonstrating a tunability range covering the entire NIR spectral window, and extending up to 5 μm in Figure 7a, it is shown the modulus of the electric field |*E*| calculated *via* COMSOL Multiphysics simulations, exciting the graphene/SiO$_2$ HMM from a vertically oriented electrical point dipole at the canalization wavelength of 4985 nm (μ_c = 0.14 eV) placed on top of the structure. The value of |*E*| along the exit layer of

the HMM is plotted in Figure 7b and fitted with a Gaussian curve. This analysis reveals a full width at half-maximum (FWHM) of ~6 nm, resulting in a remarkable confinement factor of about λ/830. The resolving power of an optical system is usually defined as the minimum distance at which two separated objects are still distinguishable.[3,51] To investigate the resolving power of the proposed HMM acting as a near-field lens, we simulated the case in which two dielectric rectangular objects are placed on top of the HMM. In particular, their interdistance is 3 nm, while their dimensions are as follows: *W* = 3 nm and *h* = 10 nm. The two objects are supposed to be made of SiO$_2$. In this case, the system is excited from a user-defined port with a mono-
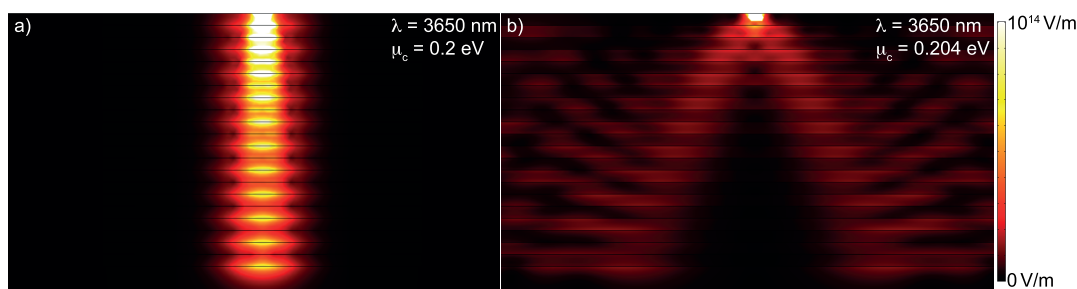
Figure 8. Propagation regime switch from (a) canalization regime (μ_c = 0.2 eV) and (b) type II anisotropy (μ_c = 0.204 eV) at 3650 nm. The type II regime is confirmed by the occurrence of the typical resonance cone pattern. Simulations are carried out by COMSOL Multiphysics, exciting with a vertically oriented dipole placed on top of the HMM.

chromatic wave at 4985 nm (μ_c = 0.14 eV) as before. The calculated |E| is shown in Figure 7c. To enhance the readability of the picture, we adopted a different color scale, whose values are mapped in the color bar placed aside. Also, we show in Figure 7d, the value of |E| all along the exit layer of the HMM. The pattern reveals the presence of two maxima whose peak-to-peak distance is equal to the center-to-center distance between the two rectangular elements. Fitting the |E| pattern with a double Gaussian curve, it is clear that the amplitude of the dip between the two Gaussian curves goes far below $1/e$, confirming that the two rectangular elements can be resolved by the HMM, down to a minimum interdistance of 3 nm. This corresponds to a resolving power of ~$\lambda/1660$. The hyper-resolution imaging properties of our structure have been further tested via 3D COMSOL simulations. In our analysis, the logo "tehris" shown in Figure 7f has been placed on top of the previous HMM and illuminated via a periodic mono-chromatic port. Here, both the thickness and the minimum width of the bar of the letter t is 10 nm. The logo is made of SiO$_2$. To show the versatility of the proposed architecture, this time we have chosen μ_c = 0.37 eV so that the canalization wavelength occurs at λ = 2054 nm. We simulated two different wavelengths: (i) 1000 nm and (ii) 2054 nm (the canalization wavelength). Despite classic optics that would predict a more than doubled resolution in this case, Figure 7g shows that it is not possible to resolve the 3D logo when illuminating with λ = 1000 nm. On the contrary, the logo is perfectly resolved if the analysis is carried out at the canalization wavelength of 2054 nm, as shown in Figure 7h. Also, in this case, a remarkable resolution of about $\lambda/200$ is demonstrated. In the end, although the HMM perfect lens is thought to be used in a steady-state configuration, the presence of graphene still allows one to switch the system on and off. The electrical gating configuration is the one described in the sketch of Figure 6d. The advantage of working across the dielectric singularity is that, as such, the canalization wavelength is extremely sensitive to any change in the dielectric permittivity of the employed materials. For example, if the chemical potential of the graphene layers is changed from 0.204 to 0.2 eV, the canalization wavelength undergoes a 65 nm blue-shift from 3650 to 3585 nm. This means that, if a graphene/SiO$_2$ HMM is used as a perfect lens at λ = 3650 nm (biased at a chemical potential of 0.2 eV), a 4 meV variation of the chemical potential of the graphene layers is sufficient to switch the behavior of the HMM at λ = 3650 nm from the canalization regime (Figure 8a) to the deep type II anisotropy, in which the near-field propagation occurs via a very characteristic pattern called resonance cones (Figure 8b).[52,53]

Moreover, even though the 1 nm SiO$_2$ layer considered here results in a relatively large capacitance value (3.5 pF), the HMM benefits of the same advantage of the configuration in Figure 3e since the series of N equal capacitances (where N is the number of bilayers by which the HMM is made of) lowers the equivalent capacitance of a factor N. The total capacitance of the HMM is therefore given by the series of the N capacitances associated to the N unit cells: C_{tot} = C/N. Considering a SiO$_2$ layer of 1 nm and a surface equal to 10^{-10} m^2 (a square of 10 10 μm ×10 μm), C_{tot} = 0.35 pF. The time constant can be calculated as expressed in eq 1, giving a switching frequency of about 500 MHz. The switching energy per bit can be calculated via eq 5 and is equal to 2.5 aJ/bit, demonstrating the possibility to achieve ~500 MHz attojoule modulation. In fact, since C_{tot} can be very small, it is plausible to expect a very small energy/bit consumption in the order of aJ, even despite the fairly high value of the back-voltage V_g. The IL and ER can be calculated directly from Figure 8b so that IL = 40 dB and ER = 26 dB. Such a high insertion loss value is given by the very reflective nature of the type II regime that attenuates the impinging radiation of 2 orders of magnitudes. On the other hand, the remarkable difference between the transmitted intensity in the canalization (Figure 8a, being the on state) and type II (Figure 8b, being the off state) regime provides a very high extinction ratio of 26. Therefore, the ER/IL figure of merit is equal to 0.65. The performances of the graphene/SiO$_2$ HMM as an electro/optical modulator working at the canalization wavelength are summarized here: switching frequency = 500 MHz, λ (nm) = 3065, V_{g-on} = 0.133 V, V_{g-off} = 0.138 V, energy/bit = 2.5 aJ/Bit, capacitance = 0.354 pF, IL = 40 dB, and ER/IL = 0.65.

It is worth saying that embedding a gain material as a dielectric layer within an HMM already demonstrated valid to increase the signal at the exit layer of the HMM.[47] Such a solution could be seen as a perspective to attenuate the high value of IL typical of this configuration.

■ MATERIALS AND METHODS

Dielectric Permittivity and Tuning of the Epsilon-Near-Zero Wavelength of Graphene. The dielectric permittivity of graphene has been calculated via the widely used Kubo formalism, reported also in Section S-1 of the Supporting Information.[54−58] All over this work, we opted for a three-sheet graphene layer, a configuration belonging to the class of the usually called "few-sheet graphene layers", whose validity in optoelectronic applications has been widely proven and which have been found able to sustain novel phenomena like tunable superconductivity in Moiré superlattices.[59−62] Moreover, a three-sheet graphene layer results in a ~1 nm-thick layer, which is very convenient for the design of metamaterial architectures, keeping our calculations in a framework of experimental feasibility. The dielectric

permittivity of a three-sheet graphene layer is shown in Figure S1a (Supporting Information) for six different chemical potentials. If the chemical potential is smaller than 0.055 eV, the real part of the dielectric permittivity of graphene is always negative. Above 0.55 eV, the real part of the dielectric permittivity crosses zero in the infrared range, reaching a propagation regime known as epsilon-near-zero.[63,64] The ENZ wavelength of graphene can be tuned by changing its chemical potential (see also Section S-1 of the Supporting Information for details), electrically doping the graphene layer applying an external voltage. The complete ENZ wavelength modification is shown in the inset of Figure S1b. Above 0.07 eV, the ENZ wavelength undergoes an exponential blue shift as the chemical potential is increased, as shown in Figure S1b.

Dielectric Permittivity of Ag and SiO$_2$. In our simulations, Ag is modeled with the well-known Drude free-electrons dispersion:[65]

$$\tilde{\varepsilon}_{Ag} = \varepsilon_\infty - \frac{\omega_p^2}{\omega^2 - i\gamma\omega} \tag{14}$$

where $\varepsilon_\infty = 5.75$, $\omega_p = 9.1$ eV, and $\gamma = 0.021$.

SiO$_2$, instead, is modeled with the Sellmeier's expression valid for the VIS-NIR range:[66]

$$\varepsilon_{SiO_2} = 1 + \left(\frac{0.6961663 \cdot \lambda^2}{\lambda^2 - 0.0684043^2}\right) + \left(\frac{0.4079426 \cdot \lambda^2}{\lambda^2 - 0.1162414^2}\right) + \left(\frac{0.8974794 \cdot \lambda^2}{\lambda^2 - 9.896161^2}\right) \tag{15}$$

Scattering Matrix Method Simulations. A standard SMM code adapted from ref 67 in MATLAB has been used.

COMSOL Simulations. Full-field simulations were carried out by exciting either with a vertically oriented dipole or with a monochromatic plane wave *via* a user-defined port, on the back of which suitably meshed perfectly matched layers have been applied. At the lateral boundaries, continuity boundary conditions were implemented to simulate infinite domains.

Lumerical Simulations. The simulation of Figure 7f,g exploits a three-dimensional finite-difference time domain (3D-FDTD) method, using a commercially available software (Lumerical), to examine the electromagnetic field distribution in the proximity of the dielectric material (SiO$_2$) placed on top of the hyperbolic metamaterial (HMM), described in our manuscript. After setting the simulation domain and the material properties, we added perfectly matched layers (PMLs) to prevent unphysical reflections from outer boundaries. The domain uses a conformal mesh, which has more accurate steps at the interfaces resolving the most critical dimensions. We defined an override mesh to adjust the mesh grid size in proximity of the pattern, which rendered a superior discretization of the physical object and improved the convergence. Three monitors across the entire simulation domain through the PMLs were placed along the orthogonal planes and used to calculate the electric field at specific point, in particular, at the HMM-dielectric surface (x–y plane), and at the two cross-sections (x–z and y–z planes) for emphasizing the canalization regime.

CONCLUSIONS

In conclusion, in this paper, we traced the route to reach a nanometric resolution in the NIR-MIR spectral range. The resolution performances in the NIR-MIR range overcome those of typical imaging apparatus in the visible range. To achieve this, we designed graphene-based metal/insulator architectures exhibiting broadband tunability by electro-chemical gating. The designed structures manifest also excellent performances as electro/optical modulators. We investigate several graphene-based metamaterial architectures with different degrees of design complexity, aiming to target specific trade-offs in terms of NIR-MIR light confinement and electro/optical modulation performances. Despite the fact that

each configuration optimizes one aspect at the expense of another, the best trade-off has been achieved in the case of a graphene/SiO$_2$ HMM working across the dielectric singularity. We provide numerical evidence that the system can be used as a tunable near-field perfect lens with a resolving power down to $\lambda/1660$ in the MIR range that allows to image 3 nm objects illuminating at a 4985 nm wavelength. To further test the imaging capabilities of this system, we investigated via COMSOL simulations a 3D framework in which the nanometric logo "tehris" has been placed on top of the same HMM. A resolution equal but not limited to $\sim\lambda/200$ is reached. The HMM featuring a dielectric singularity proved to be the perfect platform to optimize both the electrical and optical conditions to achieve ultrafast and attoJoule modulation performances. Indeed, this architecture offers the double benefit of reducing both the equivalent capacity of the modulator and the back-gate voltage switching range since, working over a resonance, a small change of the chemical potential switches the device from the canalization to a very reflective light propagation regime. These unique conditions allowed us to calculate a switching speed in the order of 500 MHz with 2.5 aJ/bit energy consumption. As a perspective, it can be noticed that the intrinsic limitations stemming from the time constant associated with the RC circuit necessary to the electrical-driven modulation can be overcome via an all-optical photogeneration of electrons and holes in graphene. The all-optical technique opens to the modulation of light intensity, polarization, and phase at terahertz frequencies.[68−70] The light confinement, resolution, broad tunability, low power consumption, and ultrafast switching properties reported in the paper make the proposed architectures the ideal platforms for both optical and non-invasive biological studies in the NIR-MIR window future developments in terahertz and new-generation optoelectronics, envisioning ultrafast and low-power all-optical switching.

■ ASSOCIATED CONTENT

ⓢ Supporting Information

The Supporting Information is available free of charge at https://pubs.acs.org/doi/10.1021/acsanm.0c02690.

> A complete calculation of the dielectric permittivity of graphene and the SMM analysis of pseudo-cavity modes occurring in a SiO$_2$/Ag bilayer (PDF)

■ AUTHOR INFORMATION

Corresponding Authors

Vincenzo Caligiuri — *Dipartimento di Fisica, Università della Calabria, Rende 87036, Italy; CNR Nanotec, Università della Calabria, Rende 87036, Italy;* ⊙ orcid.org/0000-0003-1035-4702; Email: vincenzo.caligiuri@unical.it

Roberto Caputo — *Dipartimento di Fisica, Università della Calabria, Rende 87036, Italy; Institute of Fundamental and Frontier Sciences, University of Electronic Science and Technology of China, Chengdu 610054, China;* ⊙ orcid.org/0000-0002-0065-8422; Email: roberto.caputo@unical.it

Antonio De Luca — *Dipartimento di Fisica, Università della Calabria, Rende 87036, Italy; CNR Nanotec, Università della Calabria, Rende 87036, Italy;* ⊙ orcid.org/0000-0003-2428-9075; Email: antonio.deluca@unical.it

Authors

Alessandro Pianelli − *Institute of Applied Physics, Military University of Technology, Warsaw 00-908, Poland*

Mario Miscuglio − *Department of Electrical and Computer Engineering, George Washington University, Washington, D.C. 20052, United States;* ⊙ orcid.org/0000-0001-5953-8452

Aniket Patra − *Dipartimento di Fisica, Università della Calabria, Rende 87036, Italy; Optoelectronics, Istituto Italiano di Tecnologia, Genova 16163, Italy*

Nicolò Maccaferri − *Department of Physics and Materials Science, University of Luxembourg, Luxembourg 1511 Luxembourg;* ⊙ orcid.org/0000-0002-0143-1510

Complete contact information is available at:
https://pubs.acs.org/10.1021/acsanm.0c02690

Notes

The authors declare no competing financial interest.

■ REFERENCES

(1) Liu, X.; Kuyken, B.; Roelkens, G.; Baets, R.; Osgood, R. M., Jr.; Green, W. M. J. Bridging the Mid-Infrared-To-Telecom Gap with Silicon Nanophotonic Spectral Translation. *Nat. Photonics* **2012**, *6*, 667−671.

(2) Cocorullo, G.; Della Corte, F.; Rendina, I.; Cutolo, A. New Possibilities for Efficient Silicon Integrated Electro-Optical Modulators. *Opt. Commun.* **1991**, *86*, 228−235.

(3) Kasap, S. O. *Optoelectronics and Photonics: Principles and Practices*; Prentice Hall: 2001.

(4) Soref, R. Mid-Infrared Photonics in Silicon and Germanium. *Nat. Photonics* **2010**, *4*, 495−497.

(5) Zaske, S.; Lenhard, A.; Keßler, C. A.; Kettler, J.; Hepp, C.; Arend, C.; Albrecht, R.; Schulz, W.-M.; Jetter, M.; Michler, P.; Becher, C. Visible-To-Telecom Quantum Frequency Conversion of Light from a Single Quantum Emitter. *Phys. Rev. Lett.* **2012**, *109*, 147404−147408.

(6) Smith, A. M.; Mancini, M. C.; Nie, S. Second Window for *in Vivo* Imaging. *Nat. Nanotechnol.* **2009**, *4*, 710−711.

(7) Welsher, K.; Liu, Z.; Sherlock, S. P.; Robinson, J. T.; Chen, Z.; Daranciang, D.; Dai, H. A Route to Brightly Fluorescent Carbon Nanotubes for Near-Infrared Imaging in Mice. *Nat. Nanotechnol.* **2009**, *4*, 773−780.

(8) Fischer, B. M.; Walther, M.; Jepsen, P. U. Far-Infrared Vibrational Modes of DNA Components Studied by Terahertz Time-Domain Spectroscopy. *Phys. Med. Biol.* **2002**, *47*, 3807−3814.

(9) Zhang, R.; Zhang, Y.; Dong, Z. C.; Jiang, S.; Zhang, C.; Chen, L. G.; Zhang, L.; Liao, Y.; Aizpurua, J.; Luo, Y.; Yang, J. L.; Hou, J. G. Chemical Mapping of a Single Molecule by Plasmon-Enhanced Raman Scattering. *Nature* **2013**, *498*, 82−86.

(10) Rodrigo, D.; Limaj, O.; Janner, D.; Etezadi, D.; de Abajo, F. J. G.; Pruneri, V.; Altug, H. Mid-Infrared Plasmonic Biosensing with Graphene. *Science* **2015**, *349*, 165−168.

(11) Ferguson, B.; Zhang, X.-C. Materials for Terahertz Science and Technology. *Nat. Mater.* **2002**, *1*, 26−33.

(12) Kenry; Duan, Y.; Liu, B. Recent Advances of Optical Imaging in the Second Near-Infrared Window. *Adv. Mater.* **2018**, *30*, 1802394−1802412.

(13) Anderson, R. R.; Parrish, J. A. The Optics of Human Skin. *J. Invest. Dermatol.* **1981**, *77*, 13−19.

(14) Frangioni, J. V. *In Vivo* Near-Infrared Fluorescence Imaging. *Curr. Opin. Chem. Biol.* **2003**, *7*, 626−634.

(15) Hong, G.; Antaris, A. L.; Dai, H. Near-Infrared Fluorophores for Biomedical Imaging. *Nat. Biomed. Eng.* **2017**, *1*, 1−22.

(16) Ding, F.; Zhan, Y.; Lu, X.; Sun, Y. Recent Advances in Near-Infrared II Fluorophores for Multifunctional Biomedical Imaging. *Chem. Sci.* **2018**, *9*, 4370−4380.

(17) Zoumi, A.; Yeh, A.; Tromberg, B. J. Imaging Cells and Extracellular Matrix *in Vivo* by Using Second-Harmonic Generation and Two-Photon Excited Fluorescence. *Proc. Natl. Acad. Sci.* **2002**, *99*, 11014−11019.

(18) Oka, H. Two-Photon Absorption by Spectrally Shaped Entangled Photons. *Phys. Rev. A* **2018**, *97*, 033814−033819.

(19) Schlawin, F.; Dorfman, K. E.; Mukamel, S. Entangled Two-Photon Absorption Spectroscopy. *Acc. Chem. Res.* **2018**, *51*, 2207−2214.

(20) Zhu, J.; Yan, S.; Feng, N.; Ye, L.; Ou, J.-Y.; Liu, Q. H. Near Unity Ultraviolet Absorption in Graphene Without Patterning. *Appl. Phys. Lett.* **2018**, *112*, 153106−153110.

(21) Zhu, J.; Li, C.; Ou, J.-Y.; Liu, Q. H. Perfect Light Absorption in Graphene by Two Unpatterned Dielectric Layers and Potential Applications. *Carbon* **2019**, *142*, 430−437.

(22) Bao, Z.; Wang, J.; Hu, Z.-D.; Balmakou, A.; Khakhomov, S.; Tang, Y.; Zhang, C. Coordinated Multi-Band Angle Insensitive Selection Absorber Based on Graphene Metamaterials. *Opt. Express* **2019**, *27*, 31435−31445.

(23) Feng, Y.; Hu, Z.-D.; Balmakou, A.; Khakhomov, S.; Semchenko, I.; Wang, J.; Liu, D.; Sang, T. Perfect Narrowband Absorber Based on Patterned Graphene-Silica Multilayer Hyperbolic Metamaterials. *Plasmonics* **2020**, *15*, 1869−1874.

(24) Caligiuri, V.; Dhama, R.; Sreekanth, K. V.; Strangi, G.; De Luca, A. Dielectric Singularity in Hyperbolic Metamaterials: The Inversion Point of Coexisting Anisotropies. *Sci. Rep.* **2016**, *6*, 20002−20011.

(25) Caligiuri, V.; Palei, M.; Biffi, G.; Artyukhin, S.; Krahne, R. A Semi-Classical View on Epsilon-Near-Zero Resonant Tunneling Modes in Metal/Insulator/Metal Nanocavities. *Nano Lett.* **2019**, *19*, 3151−3160.

(26) Dionne, J. A.; Sweatlock, L. A.; Atwater, H. A.; Polman, A. Planar Metal Plasmon Waveguides: Frequency-Dependent Dispersion, Propagation, Localization, and Loss Beyond the Free Electron Model. *Phys. Rev. B* **2005**, *72*, 075405−075415.

(27) Luo, S.; Wang, Y.; Tong, X.; Wang, Z. Graphene-Based Optical Modulators. *Nanoscale Res. Lett.* **2015**, *10*, 199−209.

(28) Amin, R.; Ma, Z.; Maiti, R.; Khan, S.; Khurgin, J. B.; Dalir, H.; Sorger, V. J. Attojoule-Efficient Graphene Optical Modulators. *Appl. Opt.* **2018**, *57*, D130−D140.

(29) Miller, D. A. B. Attojoule Optoelectronics for Low-Energy Information Processing and Communications. *J. Lightwave Technol.* **2017**, *35*, 346−396.

(30) Amin, R.; Maiti, R.; Gui, Y.; Suer, C.; Miscuglio, M.; Heidari, E.; Chen, R. T.; Dalir, H.; Sorger, V. J. Sub-Wavelength GHz-Fast Broadband ITO Mach−Zehnder Modulator on Silicon Photonics. *Optica* **2020**, *7*, 333−335.

(31) Karthik, R.; Akshaykranth, A. Fabrication and Modeling of Multi-Layer Metal-Insulator-Metal Capacitors. *J. Semicond.* **2017**, 123002.

(32) Caligiuri, V.; Palei, M.; Imran, M.; Manna, L.; Krahne, R. Planar Double-Epsilon-Near-Zero Cavities for Spontaneous Emission and Purcell Effect Enhancement. *ACS Photonics* **2018**, *5*, 2287−2294.

(33) Economou, E. N. Surface Plasmons in Thin Films. *Phys. Rev.* **1969**, *182*, 539−554.

(34) Caligiuri, V.; Biffi, G.; Palei, M.; Martín-García, B.; Pothuraju, R. D.; Bretonnière, Y.; Krahne, R. Angle and Polarization Selective Spontaneous Emission in Dye-Doped Metal/Insulator/Metal Nanocavities. *Adv. Opt. Mater.* **2020**, 1901215−1901220.

(35) Kuttruff, J.; Garoli, D.; Allerbeck, J.; Krahne, R.; De Luca, A.; Brida, D.; Caligiuri, V.; Maccaferri, N. Ultrafast all-optical switching enabled by epsilon-near-zero-tailored absorption in metal-insulator nanocavities. *Commun. Phys.* **2020**, *3*, 114−120.

(36) Neira, A. D.; Wurtz, G. A.; Ginzburg, P.; Zayats, A. V. Ultrafast All-Optical Modulation with Hyperbolic Metamaterial Integrated in Si Photonic Circuitry. *Opt. Express* **2014**, *22*, 10987−10994.

(37) Grinblat, G.; Abdelwahab, I.; Nielsen, M. P.; Dichtl, P.; Leng, K.; Oulton, R. F.; Loh, K. P.; Maier, S. A. Ultrafast All-Optical Modulation in 2D Hybrid Perovskites. *ACS Nano* **2019**, *13*, 9504−9510.

(38) Ermolenko, M. V.; Buganov, O. V.; Tikhomirov, S. A.; Stankevich, V. V.; Gaponenko, S. V.; Shulenkov, A. S. Ultrafast All-Optical Modulator for 1.5 μm Controlled by Ti: Al$_2$O$_3$ Laser. *Appl. Phys. Lett.* **2010**, *97*, No. 073113.

(39) Wu, Z.; Xu, Y. Design of a Graphene-Based Dual-Slot Hybrid Plasmonic Electro-Absorption Modulator with High-Modulation Efficiency and Broad Optical Bandwidth for On-Chip Communication. *Appl. Opt.* **2018**, *57*, 3260−3267.

(40) Phatak, A.; Cheng, Z.; Qin, C.; Goda, K. Design of Electro-Optic Modulators Based on Graphene-On-Silicon Slot Waveguides. *Opt. Lett.* **2016**, *41*, 2501−2504.

(41) Reed, G. T.; Mashanovich, G.; Gardes, F. Y.; Thomson, D. J. Silicon Optical Modulators. *Nat. Photonics* **2010**, *4*, 518−526.

(42) Isoniemi, T.; Maccaferri, N.; Ramasse, Q. M.; Strangi, G.; De Angelis, F. Electron Energy Loss Spectroscopy of Bright and Dark Modes in Hyperbolic Metamaterial Nanostructures. *Adv. Opt. Mater.* **2020**, *8*, 2000277.

(43) Sreekanth, K. V.; Alapan, Y.; Elkabbash, M.; Wen, A. M.; Ilker, E.; Hinczewski, M.; Gurkan, U. A.; Steinmetz, N. F.; Strangi, G. Enhancing the Angular Sensitivity of Plasmonic Sensors Using Hyperbolic Metamaterials. *Adv. Opt. Mater.* **2016**, *4*, 1767.

(44) Poddubny, A.; Iorsh, I.; Belov, P.; Kivshar, Y. Hyperbolic Metamaterials. *Nat. Photonics* **2013**, *7*, 948−957.

(45) Maccaferri, N.; Zhao, Y.; Isoniemi, T.; Iarossi, M.; Parracino, A.; Strangi, G.; De Angelis, F. Hyperbolic Meta-Antennas Enable Full Control of Scattering and Absorption of Light. *Nano Lett.* **2019**, *19*, 1851−1859.

(46) Caligiuri, V.; Pezzi, L.; Veltri, A.; De Luca, A. Resonant Gain Singularities in 1D and 3D Metal/Dielectric Multilayered Nanostructures. *ACS Nano* **2017**, *11*, 1012−1025.

(47) Caligiuri, V.; De Luca, A. Metal-Semiconductor-Oxide Extreme Hyperbolic Metamaterials for Selectable Canalization Wavelength. *J. Phys. D: Appl. Phys.* **2016**, *49*, No. 08LT01.

(48) Simovski, C.; Maslovski, S.; Nefedov, I.; Kosulnikov, S.; Belov, P.; Tretyakov, S. Hyperlens Makes Thermal Emission Strongly Super-Planckian. *Photonics Nanostruct. − Fundam. Appl.* **2015**, *13*, 31−41.

(49) Pianelli, A.; Kowerdziej, R.; Dudek, M.; Sielezin, K.; Olifierczuk, M.; Parka, J. Graphene-Based Hyperbolic Metamaterial As a Switchable Reflection Modulator. *Opt. Express* **2020**, *28*, 6708−6718.

(50) Ma, Y.; Zhi, L. Graphene-Based Transparent Conductive Films: Material Systems, Preparation and Applications. *Small Methods* **2019**, *3*, 1800199.

(51) Born, M.; Wolf, E. *Principles of Optics Electromagnetic Theory of Propagation, Interference and Diffraction of Light*; Pergamon Press: Oxford (UK), 1980.

(52) Cortes, C. L.; Newman, W.; Molesky, S.; Jacob, Z. Quantum Nanophotonics Using Hyperbolic Metamaterials. *J. Opt.* **2012**, *14*, No. 063001.

(53) de Ceglia, D.; Vincenti, M. A.; Campione, S.; Capolino, F.; Haus, J. W.; Scalora, M. Second-Harmonic Double-Resonance Cones

in Dispersive Hyperbolic Metamaterials. *Phys. Rev. B* **2014**, *89*, No. 075123.

(54) Falkovsky, L. A.; Varlamov, A. A. Space-Time Dispersion of Graphene Conductivity. *Eur. Phys. J. B* **2007**, *56*, 281−284.

(55) Koppens, F. H. L.; Chang, D. E.; García de Abajo, F. J. Graphene Plasmonics: A Platform for Strong Light-Matter Interactions. *Nano Lett.* **2011**, *11*, 3370−3377.

(56) Polini, M.; Asgari, R.; Borghi, G.; Barlas, Y.; Pereg-Barnea, T.; MacDonald, A. H. Plasmons and the Spectral Function of Graphene. *Phys. Rev. B* **2008**, *77*, No. 081411.

(57) Hanson, G. W. Dyadic Green's Functions and Guided Surface Waves for a Surface Conductivity Model of Graphene. *J. Appl. Phys.* **2008**, *103*, No. 064302.

(58) Falkovsky, L. A.; Pershoguba, S. S. Optical Far-Infrared Properties of a Graphene Monolayer and Multilayer. *Phys. Rev. B* **2007**, *76*, 153410.

(59) Nuvoli, D.; Valentini, L.; Alzari, V.; Scognamillo, S.; Bon, S. B.; Piccinini, M.; Illescas, J.; Mariani, A. High Concentration Few-Layer Graphene Sheets Obtained by Liquid Phase Exfoliation of Graphite in Ionic Liquid. *J. Mater. Chem.* **2011**, *21*, 3428−3431.

(60) Lu, L.; Ru, C. Q.; Guo, X. Vibration Isolation of Few-Layer Graphene Sheets. *Int. J. Solids Struct.* **2020**, *185-186*, 78−88.

(61) Bao, Q.; Zhang, H.; Wang, B.; Ni, Z.; Lim, C. H. Y. X.; Wang, Y.; Tang, D. Y.; Loh, K. P. Broadband Graphene Polarizer. *Nat. Photonics* **2011**, *5*, 411−415.

(62) Chen, G.; Sharpe, A. L.; Gallagher, P.; Rosen, I. T.; Fox, E. J.; Jiang, L.; Lyu, B.; Li, H.; Watanabe, K.; Taniguchi, T.; Jung, J.; Shi, Z.; Goldhaber-Gordon, D.; Zhang, Y.; Wang, F. Signatures of Tunable Superconductivity in a Trilayer Graphene Moiré Superlattice. *Nature* **2019**, *572*, 215−219.

(63) Alù, A.; Silveirinha, M. G.; Salandrino, A.; Engheta, N. Epsilon-Near-Zero Metamaterials and Electromagnetic Sources: Tailoring the Radiation Phase Pattern. *Phys. Rev. B* **2007**, *75*, 155410.

(64) Savoia, S.; Castaldi, G.; Galdi, V.; Alù, A.; Engheta, N. *PT*-Symmetry-Induced Wave Confinement and Guiding in ε-Near-Zero Metamaterials. *Phys. Rev. B* **2015**, *91*, 115114.

(65) Kittel, C. *Introduction to Solid State Physics*; 7th Ed.; Wiley: 1996.

(66) Malitson, I. H. Interspecimen Comparison of the Refractive Index of Fused Silica. *J. Opt. Soc. Am.* **1965**, *55*, 1205−1209.

(67) Rumpf, R. C. Improved Formulation of Scattering Matrices for Semi-Analytical Methods That Is Consistent with Convention. *Prog. Electromagn. Res. B* **2011**, *35*, 241−261.

(68) George, P. A.; Strait, J.; Dawlaty, J.; Shivaraman, S.; Chandrashekhar, M.; Rana, F.; Spencer, M. G. Ultrafast Optical-Pump Terahertz-Probe Spectroscopy of the Carrier Relaxation and Recombination Dynamics in Epitaxial Graphene. *Nano Lett.* **2008**, *8*, 4248−4251.

(69) Ni, G. X.; Wang, L.; Goldflam, M. D.; Wagner, M.; Fei, Z.; McLeod, A. S.; Liu, M. K.; Keilmann, F.; Özyilmaz, B.; Castro Neto, A. H.; Hone, J.; Fogler, M. M.; Basov, D. N. Ultrafast Optical Switching of Infrared Plasmon Polaritons in High-Mobility Graphene. *Nat. Photonics* **2016**, *10*, 244−247.

(70) Wagner, M.; Fei, Z.; McLeod, A. S.; Rodin, A. S.; Bao, W.; Iwinski, E. G.; Zhao, Z.; Goldflam, M.; Liu, M.; Dominguez, G.; Thiemens, M.; Fogler, M. M.; Castro Neto, A. H.; Lau, C. N.; Amarie, S.; Keilmann, F.; Basov, D. N. Ultrafast and Nanoscale Plasmonic Phenomena in Exfoliated Graphene Revealed by Infrared Pump-Probe Nanoscopy. *Nano Lett.* **2014**, *14*, 894−900.